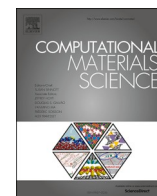| Title	Data assimilation for phase-field simulations of the formation of eutectic alloy microstructures
Author(s)	Seguchi, Yusuke; Okugawa, Masayuki; Zhu, Chuanqi et al.
Citation	Computational Materials Science. 2024, 237, p. 112910
Version Type	VoR
URL	https://hdl.handle.net/11094/95651
rights	This article is licensed under a Creative Commons Attribution 4.0 International License.
Note	

Full Length Article

Data assimilation for phase-field simulations of the formation of eutectic alloy microstructures

Yusuke Seguchi [a], Masayuki Okugawa [a,*], Chuanqi Zhu [a], Akinori Yamanaka [b], Yuichiro Koziumi [a,*]

[a] *Division of Materials and Manufacturing Science, Graduate School of Engineering, Osaka University, 2-1 Yamadaoka, Suita, Osaka 565-0871, Japan*
[b] *Department of Mechanical Systems Engineering, Tokyo University of Agriculture and Technology, 2-24-16, Naka-cho, Koganei, Tokyo 184-8588, Japan*

ABSTRACT

The phase-field (PF) method can effectively predict the formation of microstructures of eutectic alloys. However, numerous simulation parameters must be determined correctly for each alloy system to reproduce the experimentally observed microstructures. In this study, we present a data assimilation method based on an ensemble Kalman filter to determine PF simulation parameters for the directional solidification of eutectic alloy by optimizing the conditions for data assimilation. Numerical twin experiments revealed that eutectic microstructures can be reproduced, although four PF simulation parameters remained unknown. We also investigated appropriate experimental observation conditions for estimating the simulation parameters and found that the sufficient frequency of observations can be determined from the solid–liquid interfacial velocity. Our results provide guidance for data assimilation combined with the PF simulations of eutectic alloys. Moreover, our study provides a deeper understanding of the formation mechanisms of various types of eutectic microstructures.

1. Introduction

Eutectic alloys can exhibit various microstructures, such as lamellar [1,2], rod-like [3,4], and spiral [5,6] forms and the morphology significantly affect the mechanical [7,8], optical [9,10], and magnetic properties [11]. In eutectic solidification, multiphase and multicomponent are synergistic solidified under a complicated physical phenomenon involving thermal diffusions, solute diffusions, and coupled growth of different phases [12–14]. Therefore, it has long been investigated by both experimental [15–17] and computational approaches [18–21].

Phase-field (PF) simulations [22] are widely used to predict microstructure formation in various alloys [23–30] to elucidate the fundamental mechanisms of the eutectic solidification; however, many simulation parameters such as interfacial energies, interfacial mobilities, and their anisotropies must be determined through trial-and-error to reproduce experimentally observed microstructures [12–14]. In addition, the PF simulations of eutectic alloys require various simulation parameters compared to those of single-phase solidifications. Although determining such simulation parameters requires considerable time and effort, there is no guarantee that these determined simulation parameters are correct. Therefore, an efficient and reliable determination

method is required to gain a deeper understanding of the formation mechanisms of the various types of eutectic microstructures.

Recently, data assimilation (DA) methods have attracted considerable research attention for the inverse estimation of simulation parameters from observational data. Thus far, sequential and nonsequential DA have been developed. The former follows the time evolution of the ensemble, e.g., an ensemble Kalman filter (EnKF) [31], and the latter finds initial values most consistent with the observation data, e.g., a four-dimensional variational method (4D-Var) [32]. Sequential DA methods have been applied to various PF simulations, such as dendrite growth [33], solidification [34], and grain growth [35], and they have been used for estimating PF simulation parameters and evaluating estimation uncertainty. The latter has a significant advantage over nonsequential DA. Yamanaka et al. [36] applied an EnKF-based DA to multi-PF simulations of polycrystalline grain growth and succeeded in estimating the grain boundary energies. The EnKF-based DA can determine uncertainties in estimates such as interface energy and kinetic coefficient [37]. The importance of each parameter on a microstructure formation can also be evaluated from the trends of parameter changes during the estimation [35]. The DA method is effective for estimating various factors involved in the formation of complex eutectic

microstructures.

In this study, we performed DA-combined PF simulations of eutectic alloys using numerical results as synthetic observational data (i.e., twin experiments [38]) to demonstrate that the DA method can be applied to an eutectic solidification, which requires more parameters for PF simulation and more complex microstructures than those of single-phase solidification. In addition, we also investigated the effect of observation conditions on the microstructure estimation by twin experiments to propose the appropriate observation conditions toward a DA with experimental data such as the in-situ observation data of solidification [12–14].

2. Method

2.1. PF model and computational conditions

PF simulations of the directional solidification of the $MoSi_2/Mo_5Si_3$ eutectic alloy were performed using a custom-made program [39,40]. The PF model comprises two field variables: (1) PF variable ϕ, which distinguishes solid and liquid phases, and (2) concentration field c, which differs from one solid to another. ϕ was set to 0, 1, and 0.5 for the $MoSi_2$, Mo_5Si_3, and liquid phases, respectively; c ranges from 0 to 1 and represents the mole fraction of Si in the Mo–Si system. We defined these variables as $\phi(\boldsymbol{r}, t)$ and $c(\boldsymbol{r}, t)$, respectively, because they are determined by position $\boldsymbol{r} = (x, y, z)$ and time t in inhomogeneous microstructures.

The total free energy of the system is the integral of the local free energy density

$$G_{sys} = \int_V \left(g_{chem} + g_{grad} \right) dV \tag{1}$$

where g_{chem} and g_{grad} represents the chemical free energy and the gradient energy, respectively. The g_{chem} is expressed based on the Landau theory [41–43] as

$$g_{chem}(\phi, c) = \frac{A_1}{2}(c - c_1)^2 + \frac{A_2}{2}(c - c_2)\phi^2 - \frac{A_3}{4}\phi^4 + \frac{A_4}{6}\phi^6 \tag{2}$$

where c_1, c_2, and A_i represent fitting parameters. The fitted parameters are $c_1 = 0.643$, $c_2 = 0.405$, $A_1 = 3.6 \times 10^5$, $A_2 = 2.05 \times 10^5$, $A_3 = 1.26 \times 10^5$, and $A_4 = 1.16 \times 10^5$. The g_{chem} included a term to represent the double-well potential and show the local minimums of the $MoSi_2$ and Mo_5Si_3 phases with the fitted parameters, as shown in Fig. S1.

The g_{grad} is expressed using the gradients of both the concentration field and the PF variable as

$$g_{grad} = \frac{1}{2}\kappa_c^2(\nabla c)^2 + \frac{1}{2}\kappa_\phi(\theta)^2(\nabla\phi)^2 \tag{3}$$

where κ_c and κ_ϕ represent the gradient energy coefficients for concentration and PF variables, respectively. We assumed that κ_ϕ includes anisotropic interface energy depending on the interfacial normal angle from the x-axis (θ), which can be expressed as

$$\kappa_\phi(\theta) = \kappa_0[1 + \varepsilon\cos\{k(\theta - \theta_0)\}] \tag{4}$$

$$\tan\theta = \frac{\partial\phi}{\partial z}\Big/\frac{\partial\phi}{\partial x}, \ \theta = \tan^{-1}\left(\frac{\partial\phi}{\partial z}\Big/\frac{\partial\phi}{\partial x}\right) \tag{5}$$

where κ_0, ε, k, and θ_0 represent the mean value of the gradient energy coefficient, strength of anisotropy, order of rotational symmetry, and original angle of the rotation, respectively [39,40].

The time evolution of the concentration and PF variables is calculated using the Cahn–Hilliard (**Eq. (6)**) and Allen–Cahn (**Eq. (7)**) equations [44,45]

$$\frac{\partial c}{\partial t} = \nabla\left[M_c\left(\nabla\frac{\delta G_{sys}}{\delta c}\right)\right], \tag{6}$$

$$\frac{\partial\phi}{\partial t} = -m_\phi\frac{\delta G_{sys}}{\delta\phi} \tag{7}$$

where M_c and m_ϕ represent the mobilities for the order parameters of c and ϕ, respectively. It is noted that the m_ϕ is phase-field mobility, which is a component of interface mobility given by $2 m_\phi\kappa$, where κ is the gradient energy coefficient.

The simulation domain is two-dimensional (128 μm × 128 μm and 128 × 128 meshes; $\Delta x = 1$ μm). Table 1 lists the PF simulation parameters; all parameters used in the PF simulations are non-dimensionalized in terms of the gas constant (8.3145 J·K^{-1}·mol^{-1}), eutectic temperature (2173 K), mesh size ($\Delta x = 1$ μm), and diffusion coefficient in the liquid phase ($D_L = 2.46 \times 10^{-8}$ m^2·s^{-1}). Neumann and Dirichlet boundary conditions are set for the bottom and top of the solidification direction, i.e., $y = 0$ μm and $y = 128$ μm, respectively, and the periodic boundary conditions are set for the others. The domain is set to the liquid phase ($\phi = 0.5$) with $c = 0.55$, and the temperature of the bottom of the domain is set to the eutectic temperature (2173 K). The computational domain is solidified directionally under the conditions of the temperature gradient $G = 1.57 \times 10^5$ K·m^{-1} and solidification rate $R = 34.8$ mm·h^{-1}.

2.2. DA based on EnKFs

Fig. 1 schematically illustrates the EnKF calculation process. In sequential DA methodologies [33–38], we define a state vector ξ_t containing all state variables at t as

$$\xi_t = \begin{bmatrix} \phi_{1,1} \\ \vdots \\ \phi_{N,M} \\ c_{1,1} \\ \vdots \\ c_{N,M} \end{bmatrix} \tag{8}$$

where $\phi_{n,m}(1 \leq n \leq 128, 1 \leq m \leq 128)$ represents the PF variable on a different grid point (n,m) at t. In this study, ξ_t represents a vector containing ϕ and c on each grid point of the whole computational domain. The numerical simulation was updated using ξ_t from a state vector at time t_{n-1} to a state vector at t_n.

$\boldsymbol{\Psi}_t$ is a vector consisting of estimated parameters, and we define an augmented state vector $\boldsymbol{x}_t$, including the state vectors containing ξ_t and $\boldsymbol{\Psi}_t$. This vector is expressed as

$$\boldsymbol{x}_t = \begin{bmatrix} \boldsymbol{\xi}_t \\ \boldsymbol{\Psi}_t \end{bmatrix} \tag{9}$$

The time evolution of $\boldsymbol{x}_t$ is calculated by solving

$$\boldsymbol{x}_t = f_t(\boldsymbol{x}_{t-1}) + \boldsymbol{v}_t \tag{10}$$

where f_t represents a nonlinear operator that corresponds to the time evolution equations of the two field variables, that is, **Eqs. (6) and (7)**,

Table 1
Parameters used of the phase-field simulation.

Parameter	Value
Si concentration of initial liquid phase, c_0	55 at.%
Simulation area	128 μm × 128 μm
Grid number	128 × 128
Time step, Δt	0.001 s* (6.6 × 10^{-4} s)
Interface thickness, λ	2 nm
Temperature, T	2173 K
Solidification rate, R	34.8 mm·h^{-1}
Temperature gradient, G	3.13 × 10^5 K·m^{-1}
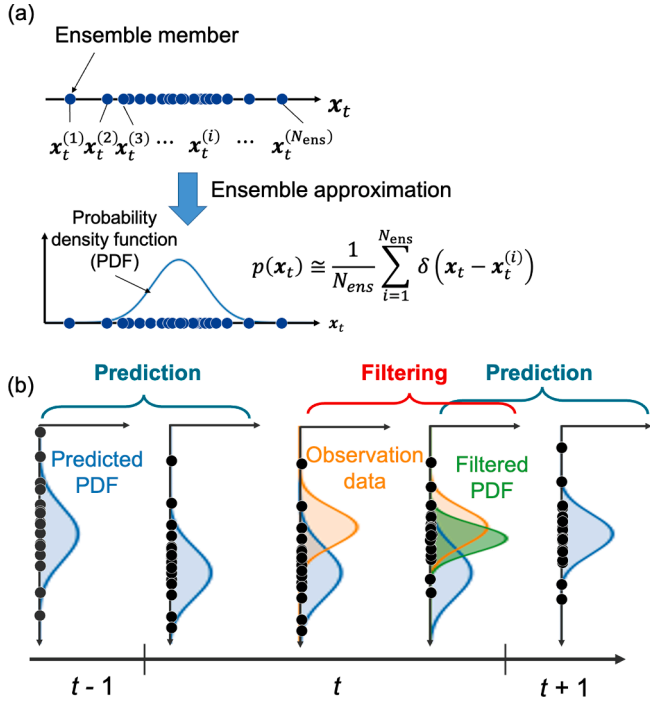
Fig. 1. (a) Ensemble approximation of probability density function and (b) approximating the probability density function (PDF) from the sparsity of ensemble members. Track the time evolution of the PDF by solving the time evolution equation for each ensemble member (Prediction) and correct it using observation data estimation (Filtering). The true state is estimated by iteratively performing prediction and filtering.

respectively. The additional term $\mathbf{v}_t$ is called the system noise and represents the imperfectness of the simulation.

We define an observation vector $\mathbf{y}_t$ containing the observation data, which can be expressed as

$$\mathbf{y}_t = \mathbf{H}_t \mathbf{x}_t + \mathbf{w}_t \tag{11}$$

where $\mathbf{H}_t$ represents an observation operator that transforms the state variable vector of the model $\mathbf{x}_t$ into an observation equivalent vector $\mathbf{y}_t$ of the same dimension as the observation vector $\mathbf{y}_t^{\mathrm{obs}}$ that lines up the observed data, and $\mathbf{w}_t$ represents the observation noise which is an error included in the experimental data.

2.3. EnKF

An EnKF is adapted in this study to handle nonlinear simulation models [39,40]. Several simulations with different simulation parameters are executed in parallel to compute the time evolution of the probability density function (PDF) $p(\mathbf{x}_t)$, which is approximated using an ensemble approximation as

$$p(\mathbf{x}_t) \cong \frac{1}{N_{\mathrm{ens}}} \sum_{i=1}^{N_{\mathrm{ens}}} \delta\left(\mathbf{x}_t - \mathbf{x}_t^{(i)}\right) \tag{12}$$

where $\delta(x)$ represents the Dirac delta function, and N_{ens} represents the number of model states (also called ensemble size). The ensemble size in the EnKF-based DA corresponds to the number of parallel-running PF simulations.

The predictive PDF is updated by phase field simulations of individual ensemble members. The time evolution to time t of the state vector $\mathbf{x}_{t|t-1}^{(i)}$ for the i-th ensemble member assimilated with the observed data up to t-1 is expressed as

$$\mathbf{x}_{t|t-1}^{(i)} = f_t\left(\mathbf{x}_{t-1|t-1}^{(i)}\right) + \mathbf{v}_t^{(i)} \tag{13}$$

where $\mathbf{v}_t^{(i)}$ denotes the system noise of the i-th ensemble and f_t represents the function to forward in time (i.e., **Eqs. (6) and (7)**).

When the observed data exist, the filter PDF is updated based on Bayes' theorem using the likelihood function corresponding to the observation data and the predictive PDF. Meanwhile, individual ensemble members are filtered by the observation data based on Bayes' theorem.

$$\mathbf{x}_{t|t}^{(i)} = \mathbf{x}_{t|t-1}^{(i)} + \mathbf{K}_t\left(\mathbf{y}_t^{\mathrm{obs}} + \widetilde{\mathbf{w}_t^{(i)}} - \mathbf{H}_t \mathbf{x}_{t|t-1}^{(i)}\right) \tag{14}$$

where $\mathbf{y}_t^{\mathrm{obs}} + \widetilde{\mathbf{w}_t^{(i)}}$ corresponds to the perturbed observation. The parameter $\widetilde{\mathbf{w}_t^{(i)}}$ is added to prevent underestimating the filter PDF covariance matrix $\mathbf{P}_{t|t}$ when using the same observation state vector $\mathbf{y}_t^{\mathrm{obs}}$ for each ensemble member. Eq. (14) represents a modification of each ensemble member $\mathbf{x}_{t|t-1}^{(i)}$ using the observation data. $\mathbf{K}_t$ is called the Kalman gain and is given by

$$\mathbf{K}_t = \mathbf{P}_{t|t-1}\mathbf{H}_t^T\left(\mathbf{H}_t\mathbf{P}_{t|t-1}\mathbf{H}_t^T + \mathbf{R}_t\right)^{-1} \tag{15}$$

where $\mathbf{P}_{t|t-1}$ represents a predictive PDF covariance matrix, which can be calculated as

$$\mathbf{P}_{t|t-1} = \frac{1}{N_{\mathrm{ens}}-1} \sum_{i=1}^{N_{\mathrm{ens}}} \widetilde{\mathbf{x}_{t|t-1}^{(i)}}\left(\widetilde{\mathbf{x}_{t|t-1}^{(i)}}\right)^T, \tag{16}$$

$$\widetilde{\mathbf{x}_{t|t-1}^{(i)}} = \mathbf{x}_{t|t-1}^{(i)} - \frac{1}{N_{\mathrm{ens}}} \sum_{i=1}^{N_{\mathrm{ens}}} \mathbf{x}_{t|t-1}^{(i)} \tag{17}$$

The time evolution of the sample covariance matrix $\mathbf{P}_{t|t-1}$ is given as

$$\mathbf{P}_{t|t} = \mathbf{P}_{t|t-1} - \mathbf{K}_t\mathbf{H}_t\mathbf{P}_{t|t-1}. \tag{18}$$

The observation error covariance matrix $\mathbf{R}_t$ is given as

$$\mathbf{R}_t = \frac{1}{N_{\mathrm{ens}}-1} \sum_{i=1}^{N_{\mathrm{ens}}} \widetilde{\mathbf{w}_t^{(i)}}\left(\widetilde{\mathbf{w}_t^{(i)}}\right)^T. \tag{19}$$

$$\widetilde{\mathbf{w}_t^{(i)}} = \mathbf{w}_t^{(i)} - \frac{1}{N_{\mathrm{ens}}} \sum_{i=1}^{N_{\mathrm{ens}}} \mathbf{w}_t^{(i)} \tag{20}$$

In this study, a true state is estimated by repeating the filtering processes and comparing the observation data and predicted states calculated by the PF simulation using the predicted parameters. For comparison, the means and standard deviations (SDs) of the ensemble of the observation data and predicted states are evaluated. The means were calculated as

$$\bar{\mathbf{x}}_{t|t-1} = \frac{1}{N_{\mathrm{ens}}} \sum_{i=1}^{N_{\mathrm{ens}}} \mathbf{x}_{t|t-1}^{(i)}. \tag{21}$$

On the other hand, SD of the ensemble is the square root of the diagonal elements of the covariance matrix represented by

$$\mathbf{P}_{t|t-1} = \frac{1}{N_{\mathrm{ens}}-1} \sum_{i=1}^{N_{\mathrm{ens}}} \left(\mathbf{x}_{t|t-1}^{(i)} - \bar{\mathbf{x}}_{t|t-1}\right)\left(\mathbf{x}_{t|t-1}^{(i)} - \bar{\mathbf{x}}_{t|t-1}\right)^T \tag{22}$$

2.4. Twin experiments

Twin experiments were conducted to validate the DA method. Fig. 2 shows the flowchart of the twin experiment in the present study. Originally, DA is performed using experimentally observed data. In the twin experiments, simulation results are used instead of experimental data. First, the PF simulation was performed using the true values of the
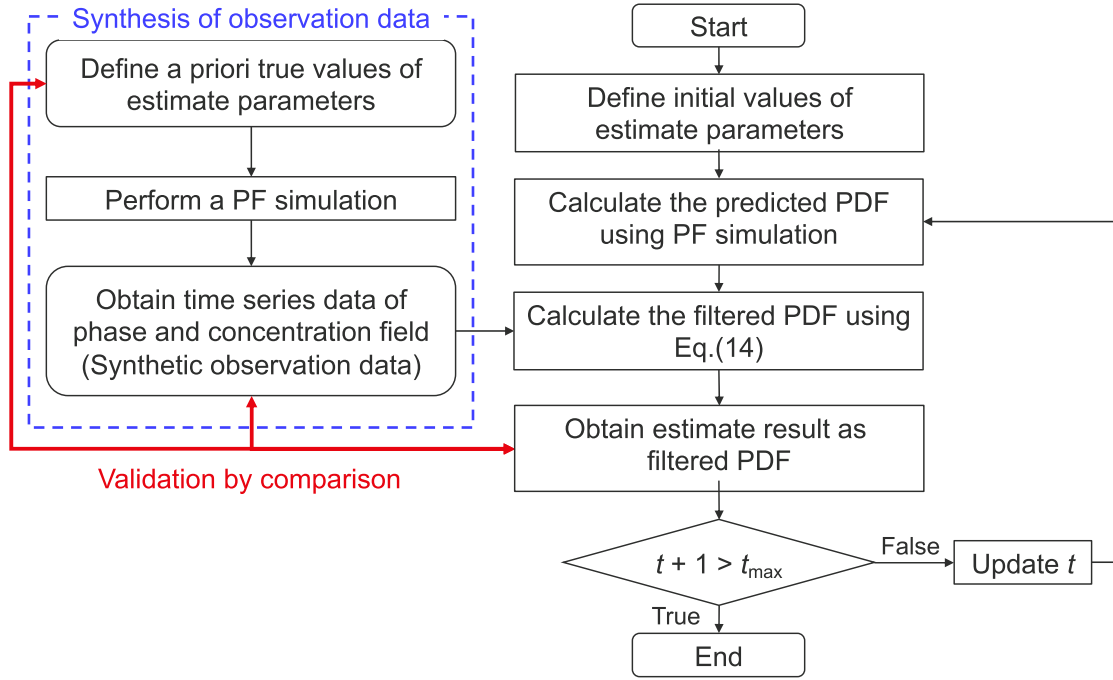
Fig. 2. Flowchart of the twin experiment using the EnKF.

parameters to be estimated, and time series data of the phase distribution were obtained. The EnKFs were performed using the pseudo-observed data: the time evolution of the predicted PDF was calculated by the PF simulations for each ensemble member, and the predicted PDF was filtered using the pseudo-observation data. Finally, we evaluate the estimation accuracy of the DA by comparing the estimated parameter with the true values of the parameters and the estimated state with the pseudo-observed data, respectively.

PF simulations were performed assuming a priori true values and used as synthetic observations. The parameters were then estimated by data assimilation, assuming that the true values were unknown. For the PF simulations generating the pseudo-observational data, we configured the dimensionless computational parameters as follows: PF mobility $m_\phi = 2.5$, solute mobility $M_c = 2.5$, anisotropy strength $\varepsilon = 0.3$, gradient energy coefficient $\kappa_0 = 0.82$. In this study, the above four computational parameters were inversely estimated from the phase distribution. We used the pre-computed PF variables $\phi(\boldsymbol{r}, t)$ as pseudo-observation data and PF variables $\phi(\boldsymbol{r}, t)$ and concentration field $c(\boldsymbol{r}, t)$ are used as the true state for validation by comparing it with simulation results obtained using the estimated simulation parameters. The observation matrix $\boldsymbol{H}_t$ used in this study has a dimension of $1 \times (2 \times 128 \times 128 + 4)$, and its first 128×128 components are 1 and the others are zeros. The observation vector $\boldsymbol{y}_t$ is expressed as

$$\boldsymbol{y}_t = \begin{bmatrix} \phi_{1,1} & \cdots & \phi_{n,m} & \cdots & \phi_{128,128} \end{bmatrix}^T. \tag{23}$$

This parameter is a real number with values between 0 and 1. This can be considered the phase of each observation point in the actual experimental data. The argument state vector of the i-th ensemble member is given by

$$\boldsymbol{x}_t^{(i)} = \begin{bmatrix} \boldsymbol{\xi}_t^{(i)} \\ \boldsymbol{\Psi}_t^{(i)} \end{bmatrix}, \tag{24}$$

where $\boldsymbol{\xi}_t^{(i)}$ and $\boldsymbol{\Psi}_t^{(i)}$ are calculated using

$$\boldsymbol{\Psi}_t^{(i)} = \begin{bmatrix} m_{\phi,t}^{(i)} & M_{c,t}^{(i)} & \kappa_t^{(i)} & \varepsilon_t^{(i)} \end{bmatrix}^T, \tag{25}$$

where m_ϕ, M_c, $\kappa(=\kappa_0 = \kappa_c)$, and ε represent the PF interface mobility, solute mobility, gradient energy coefficient, and anisotropy intensity of gradient energy coefficient, respectively. The time evolution of the PF interface mobility $m_{\phi,t}^{(i)}$ can be expressed as

$$m_{\phi,t}^{(i)} = m_{\phi,t-1}^{(i)} + v_{t,m_\phi}^{(i)}. \tag{26}$$

$v_{t,m_\phi}^{(i)}$ is given by

$$v_{t,m_\phi}^{(i)} \quad N\left(0, \sigma_{\mathrm{sys}}^{m_\phi\,2}\right) \tag{27}$$

where N indicates the Gaussian distribution. **Eq. (26)** indicates that $v_{t,m_\phi}^{(i)}$ represents the system noise of m_ϕ, which is a random variable following a Gaussian distribution with mean zero and standard deviation $\sigma_{\mathrm{sys}}^{m_\phi}$. The other parameters are described in the same manner.

EnKF has seven DA conditions: ensemble size N_{ens}, filtering interval Δt_{filt}, number of simulation parameters to estimate n_{para}, initial mean μ_{init} and initial standard deviation σ_{init} of the DA conditions, system noise σ_{sys}, and observation noise σ_{obs}. In this study, n_{para} and σ_{obs} are fixed at 4 and 0.01, respectively. The initial standard deviations σ_{init} of DA conditions and system noise σ_{sys} are set to 10 % and 1 % of the initial means μ_{init}, respectively. The initial mean values of parameters were set as follows: PF mobility $m_{\phi,\mathrm{init}} = 2$, solute mobility $M_{c,\mathrm{init}} = 2$, anisotropy strength $\varepsilon_{\mathrm{init}} = 0.2$, gradient energy coefficient $\kappa_{0,\mathrm{init}} = 1.4$. Among the DA conditions of EnKF, N_{ens} and Δt_{filt} are optimized because they directly determine the accuracy of the estimation.

3. Results and discussion

3.1. Applicability of the DA combined PF model to eutectic solidification verified by twin experiments

The validity of the DA for eutectic alloy solidification was investigated by a twin experiment using the different ensemble sizes, N_{ens}, which is the number of parallel-running simulations required to approximate the PDF and is one of the hyperparameters of the EnKF-

based DA. The resulting eutectic microstructures colored according to the values of $\Phi(r, t)$ and $c(r, t)$ are shown in Fig. 3 The averaged phase distribution largely depends on the N_{ens}. In the simulation with $N_{\text{ens}} = 20$, the eutectic microstructure growth stopped before solidifying the entire domain in the simulation. Furthermore, the simulation collapsed when N_{ens} was 50. In contrast, simulations with $N_{\text{ens}} = 100$ and 200 reproduced the assumed true state.

Fig. 3(b1)–(b4) show the time variations of the mean and standard deviations (SDs) of the estimated simulation parameters during DA. The estimated values for $N_{\text{ens}} = 20$ and 50 deviated significantly from the true values; however, the estimated values for $N_{\text{ens}} = 100$ and 200 approached the true values at the beginning of the simulation and remained near the true values throughout the simulations. Filter divergence, which is a phenomenon of bias in the extracted samples when approximating a PDF with an ensemble, occurred in simulations with $N_{\text{ens}} = 20$ and 50. Sasaki et al. [38] suggested that filter divergence can be avoided by increasing N_{ens}. This is because the larger N_{ens} is, the less likely the extracted samples will be biased and the more accurate the PDF approximation will be. However, an appropriate N_{ens} is required,

given that the computational cost is limited in practical use. These twin experiments revealed that estimation through the DA for eutectic solidification is possible for ensemble sizes $N_{\text{ens}} = 100$ or larger. In previous studies on DA-combined PF simulations of single-phase solidifications [34,37], $N_{\text{ens}} = 100$ is sufficient to estimate the parameters of the PF simulation. This implies that the required N_{ens} of this study for the DA of the eutectic alloy solidification is the same as that of single-phase solidifications [34,37].

Fig. 4(a) shows the SD of the estimated concentration field at 9,000 steps under different ensemble size conditions. As indicated in Fig. 4(a), increasing the ensemble size leads to higher accuracy in parameter estimation. The SD of the concentration field estimation for $N_{\text{ens}} = 100$ is smaller than that for $N_{\text{ens}} = 200$. It is suggested [46,47] that the diffusion distance of solute atoms per time step is required to be smaller than the square of Δx for calculating the time evolution of the concentration field stably; increasing solute mobility M_c under constant Δt and Δx causes the calculation to become unstable. Fig. 4(b) shows the concentration field obtained in PF simulations without EnKF applied using various M_c. Discontinuous regions appear in the concentration field, i.e.,
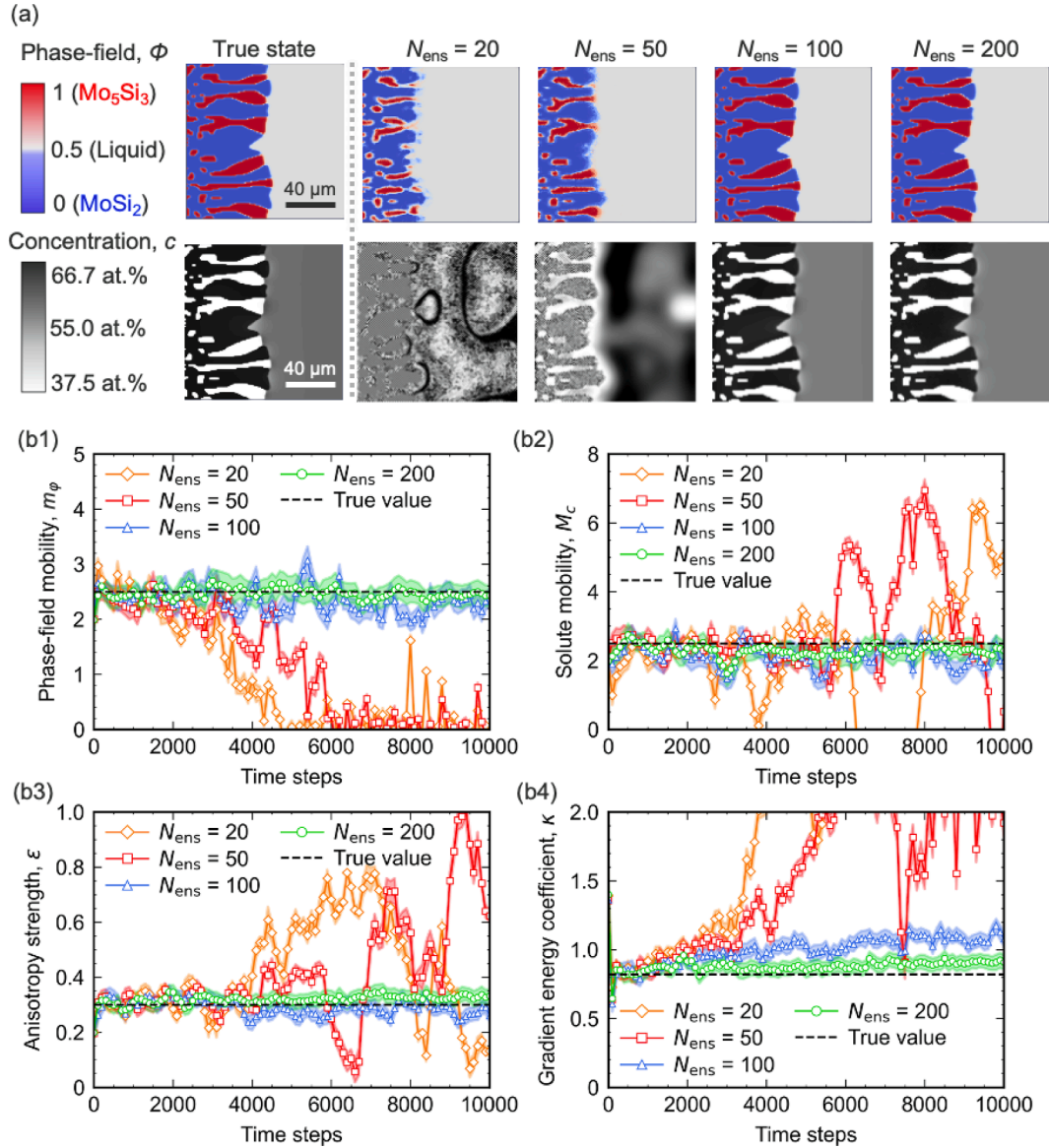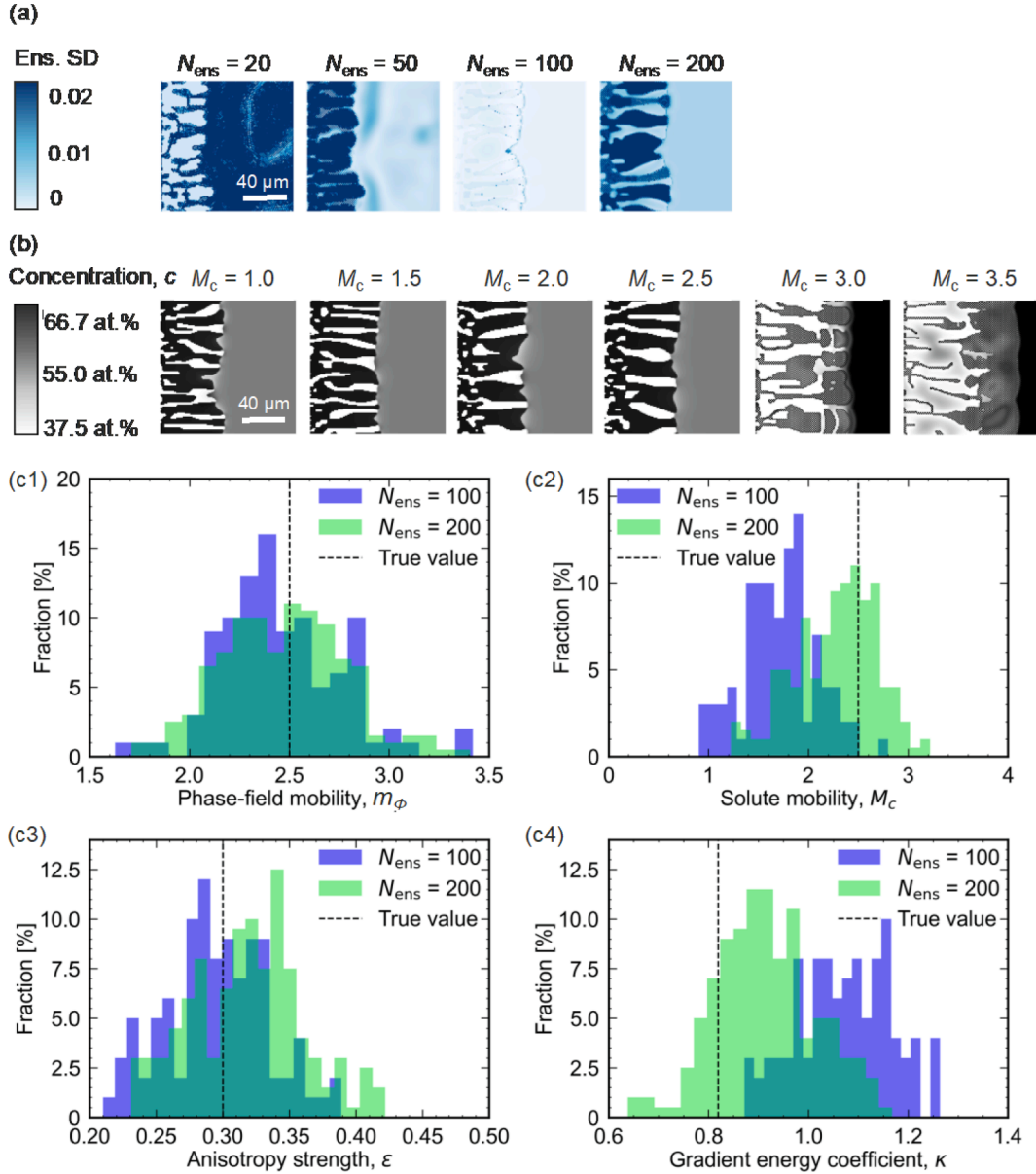

Fig. 3. (a) Distributions of PF variables and concentration at 9000 steps of synthetic observation data (true state) and EnKF estimated states with $N_{\text{ens}} = 20, 50, 100,$ and 200. Time variations of ensemble mean and SD of (b1) phase-field mobility, (b2) solute mobility, (b3) anisotropy strength, and (b4) gradient energy coefficient during DA.

(a)

(b)

Fig. 4. (a) SDs in concentration fields estimated with ensemble size estimated N_{ens} as 20, 50, 100, and 200. (b) Concentration fields calculated using solute mobility $M_c = 1.0$–3.5. The variation of estimated (c1) phase-field mobility, (c2) solute mobility, (c3) anisotropy strength, and (c4) gradient energy coefficient at 9000 steps.

the calculation is unstable when using a larger M_c than 3.0. Comparing the solute mobility distributions for $N_{ens} = 100$ and 200 at 9,000 steps indicated in Fig. 4(c), only $N_{ens} = 200$ has ensemble members with an M_c larger than 3.0. Therefore, it is suggested that the concentration field was unstable for these ensemble members and caused the larger SD in the concentration field estimation for $N_{ens} = 200$ compared to $N_{ens} = 100$.

3.2. Consideration of effects of observation conditions on the microstructure estimation

In the previous studies, in-situ observation of microstructure formations has been performed using optical microscope [12,48–52], X-ray imaging [15,53–57], and dynamic transmission electron microscope (DTEM) [58–61]. Optical microscopes are most commonly used tool for observations and can observe a several mm-squared space with a spatial resolution on the order of μm and temporal resolution on the order of tens fps. Witusiewicz et al. [50,51] observed the solidification of eutectic alloys with the low-eutectic temperatures such as the neopentylglycol-

(D)camphor eutectic alloy and the Al-based alloy using the optical microscope. X-ray imaging allows in-situ observation in higher temperature conditions. In addition, concentration distribution changes can also be tracked by X-ray fluorescence spectroscopy [55,56]. Yasuda et al. [57] observed the solidification of the low carbon steel with a spatial resolution of 5 μm and a temporal resolution of 32 fps using the X-ray imaging. On the other hand, DTEM can track nanosecond order temporal changes with a spatial resolution on the order of nm, while the observation field of view is limited up to 100 μm and it is applicable only to thin film samples [59]. Microstructure formation of the Al eutectic alloys under the fast solidification conditions considering the additive manufacturing process has been studied using the DTEM technique [59–61]. The field of view and spatiotemporal resolutions differ greatly depending on the method, and an appropriate method is necessary to be chosen for the structural morphology to be observed.

In this study, we investigated the applicability of the DA combined PF simulation to a two-dimensional optical microscope observation of the eutectic solidification such as that by Chuang et al. [52]. We considered the effect of filtering interval Δt_{filt} on microstructure

estimation; the estimation accuracy in DA improves because of more opportunities for modifications based on observation data when the frequency of observations is high. However, in actual experiments, the frequency of observations remains limited. Chuang et al. [52] observed the in-situ directional solidification of the eutectic alloy with a spatial resolution of 1.56 μm and a frame rate of 30 fps (temporal resolution = 33 ms). To revealed the effect of Δt_{filt} on the estimation accuracy, we performed the DA combined PF simulations with a spatial resolution of 1 μm for different Δt_{filt} steps of 30, 50, 100, and 200, which correspond to 19.8, 33, 66, and 132 ms, respectively. The PF simulations are performed again using the estimated values, and the obtained $\phi(\boldsymbol{r}, t)$ and c $(\boldsymbol{r}, t)$ are compared with the true values. The ensemble size N_{ens} was fixed to 100 for all twin experiments.

Fig. 5(a) shows the simulated eutectic microstructures using different Δt_{filt} of 200, 100, 50, and 30 steps. The assumed true state was reproduced in the simulations using Δt_{filt} of 100, 50, and 30 steps (except for Δt_{filt} = 200 steps). The time variations of the mean and standard deviation for the estimated simulation parameters during DA were calculated, as shown in Fig. 5(b1)–(b4). The estimated values for

Δt_{filt} = 200 deviated significantly from the true values. However, the estimated values with Δt_{filt} = 100, 50, and 30 steps remained closer to the true values during the entire simulation. The estimated simulation parameters at 9000 steps were compared to evaluate the effect of Δt_{filt} on the estimation of the simulation parameters. The Δt_{filt} is the time interval during which the simulation results are modified with observation data, and its inverse corresponds to the frequency of experimental observations. The estimation accuracy improves as the observation frequency increases. Therefore, by obtaining observation data at a higher frequency and modifying the simulation results successively with more observation data, the parameters can be inversely estimated from the microstructure time series data with higher accuracy.

The PF simulations were performed again using the estimated simulation parameters at 9000 steps (Table 1) to verify the reproducibility of the assumed true state. Fig. 6(a) shows the resulting eutectic microstructures colored according to the values of $\phi(\boldsymbol{r}, t)$ and $c(\boldsymbol{r}, t)$. The measured area ratios and lamellar spacings of each model are shown in Fig. 6(b1)–(b3). No lamellar structure was formed in the simulation with Δt_{filt} = 200 steps, and thus, this simulation was excluded from the
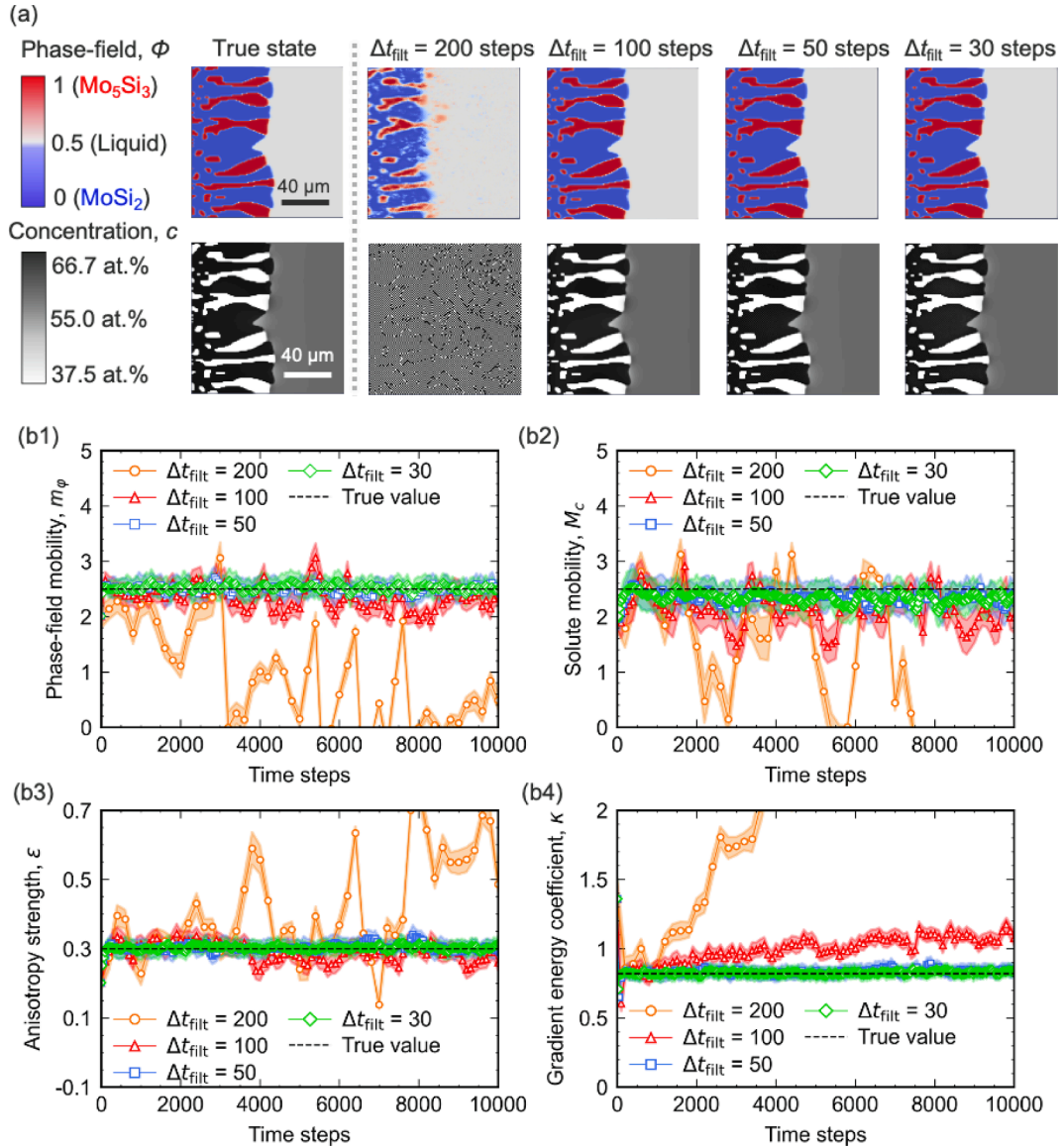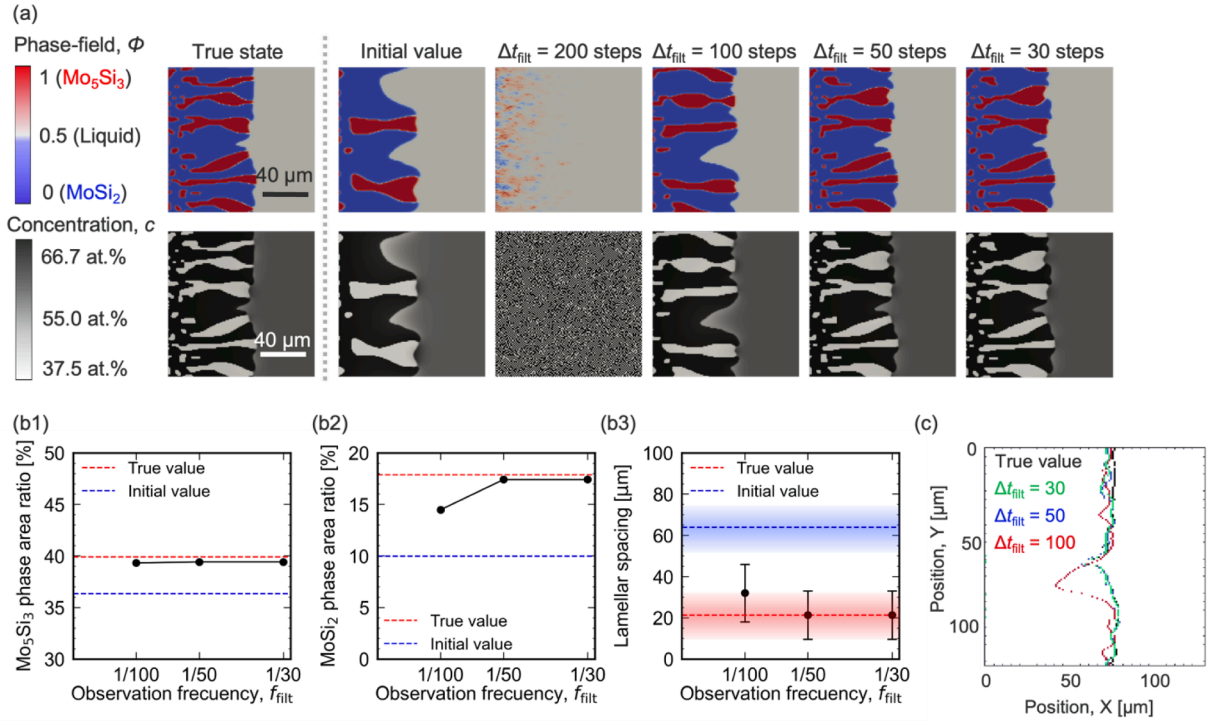

Fig. 5. (a) Distributions of PF variables and concentration at 9000 steps of synthetic observation data and EnKF estimated states with filtering interval Δt_{filt} = 200, 100, 50, and 30 steps. Time variations of ensemble mean and SD of (b1) phase-field mobility, (b2) solute mobility, (b3) anisotropy strength, and (b4) gradient energy coefficient during DA.

Fig. 6. (a) Distributions of PF variables and concentration at 10,000 steps obtained by PF simulations using the initial and determined parameters of DA combined PF simulations. (b) Area fraction of (b1) Mo_5Si_3 and (b2) $MoSi_2$ phases and (b3) average lamella spacing of the eutectic microstructures. (c) Comparison of the simulated solid–liquid interface positions for the cases with $\Delta t_{filt} = 30$, 50, and 100 steps.

comparison. The fractions of solid phases (Fig. 6(b1)) were smaller than those simulated using the true simulation parameters because PF mobility m_ϕ and solute diffusion mobility M_c could be underestimated (Table 2). Small mobilities slowed the solid–liquid interfacial migration and solute diffusion, as shown in Fig. 6(c). Thus, the interface has a convex shape, which decreases the solid-phase fraction. The lamellar spacings obtained from simulations using the estimated PF simulation parameters with $\Delta t_{filt} = 50$ and 30 steps were almost the same as the true values, while those obtained from simulations with $\Delta t_{filt} = 100$ steps were larger than the true value (Fig. 6(b3)). This was because κ is slightly larger than those in the other two simulations at $\Delta t_{filt} = 100$ steps (Table 1). Owing to the overestimated κ, the interfacial energy of the microstructure became large and energetically unstable in the early stages of solidification. Thus, the microstructure disappeared, and the lamellar spacing increased. Therefore, it was determined that $\Delta t_{filt} = 100$ steps was not sufficient for accurate parameter estimation to reproduce microstructure formation, and Δt_{filt} should be less than 50 steps. Here, 50 steps in the calculation is 0.033 s in real time, and a filtering interval of 0.033 s corresponds experimentally to 31 observations per second.

Based on the simulation results obtained using different Δt_{filt}, an in-situ observation movie with an observation frequency of above 31 fps was suggested for use in the EnKF-based DA combined PF simulations to reproduce an actual microstructure formation of eutectic alloys. Chuang

et al. [52] observed the directional solidification of the eutectic alloy with a frame rate of 30 fps. DA-combined PF simulations with experimental in-situ observation data were suggested to reproduce an experimental microstructure and estimate parameters for PF simulations.

The results of this study with different Δt_{filt} were compared with the results of previous studies [34,37], in which the same DA method was used to provide a guideline to determine Δt_{filt} for DA. Table 3 lists the estimation conditions used in this study and in the previous studies [34,37]. The values of Δt_{filt} used in previous studies were 10 times larger than those used in this study. The speeds of the solid–liquid interfacial migration ($V_{interface}$) in this study and previous studies were different. Therefore, we defined $V_{filt} = \Delta t_{filt} \times V_{interface}$, where V_{filt} represents the distance where the solid–liquid interface moves from one filter to

Table 2
Parameters used for phase-field simulation to reproduce the observation data with estimated parameters.

Parameter	Δt_{filt} = 30 steps	Δt_{filt} = 50 steps	Δt_{filt} = 100 steps
PF mobility, m_ϕ	2.46	2.45	2.49
Solute mobility, M_c	2.44	2.37	1.83
Anisotropy strength, ε	0.302	0.302	0.287
Gradient energy coefficient, κ_0	0.827	0.845	1.07

Table 3
Comparison of estimation conditions between the present and previous studies.

Parameter	This study	Ref. 34	Ref. 37
Alloy system	Eutectic alloy	Pure metal	Pure metal
Computational Domain	128 × 128	100 × 100	128 × 128
Number of state variables	2	1	1
Estimated parameters	PF mobility m_ϕ, solute mobility M_c, gradient energy coefficient κ_0, and its anisotropy ε	Kinetic coefficient β_0 and its anisotropy ε_k, interfacial energy σ_0 and its anisotropy ε_c	Kinetic coefficient β_0 and its anisotropy ε_k, interfacial energy σ_0 and its anisotropy ε_c
Dimension of state vector	32,772	10,004	16,386
Ensemble number, N_{ens}	100	100	512
Time step, Δt	6.6×10^{-4} s	1.00×10^{-14} s	1.00×10^{-14} s
Filtering step, Δt_{filt}	6.6×10^{-2} s	1.00×10^{-11} s	1.00×10^{-11} s
Filtering step, Δt_{filt} /Δt	100 steps	1000 steps	1000 steps

another. In this study, 16,000 steps were required for the solid–liquid interface to pass through the 128×128 computational domains. The corresponding $V_{\text{interface}}$ was 8.0×10^{-3} grid·step^{-1}, and V_{filt} were calculated to be the 1.6, 0.8, 0.4, and 0.24 grid filtering step^{-1} for the Δt_{filt} of 200, 100, 50, and 30 steps, respectively. $V_{\text{interface}}$ and V_{filt} in the previous studies [34,37] were 8×10^{-4} and 5×10^{-4} grid·step^{-1} and 0.8 and 0.5 grid filtering step^{-1}, respectively. Fig. 7 shows the relationship between the estimation accuracy and V_{filt}. The estimation accuracy changes significantly around $V_{\text{filt}} = 1$, and a correct estimation is achieved when $V_{\text{filt}} < 1$. Therefore, the condition $V_{\text{filt}} < 1$ is necessary for estimating the PF simulation parameters governing the interfacial migration using the growing phase morphology as the observation data.

The coefficient of variation (CVs) and ratio of standard deviation to the mean of the estimated PF simulation parameters were calculated to evaluate the contribution of each parameter to the microstructure formation. Fig. 8 shows the CV over time for the simulations with $\Delta t_{\text{filt}} = 100$, 50, and 30 steps. The CVs of M_ϕ and κ coefficients exhibited almost the same values. Moreover, the CV of the solute mobility was the largest through each simulation, and that of the anisotropy strength was the smallest. Miyoshi et al. [35] noted that the uncertainty of the estimate is large for grain boundary mobility of relatively immobile grain boundaries. This suggests that the smaller the contribution of a parameter to the phenomenon, the larger the uncertainty of the estimate. In this study, the CV corresponds to the uncertainty, suggesting that the anisotropy strength with the smallest CV has the largest contribution to microstructure formation. From another perspective, a parameter with a significant contribution to the observation data should be appropriately determined to apply the DA method to experimental observations.

Selecting in-situ observation data largely affected by DA conditions to be determined is necessary.

4. Conclusion

A twin experiment was conducted to demonstrate the verification of EnKF applied to a PF simulation of eutectic solidification. The PF mobility, solute mobility, gradient energy coefficient, and anisotropic strength were estimated simultaneously using the optimized DA conditions.

The PF simulations of eutectic alloys require more phases and complex shapes than those of a single-phase solidification. Estimating the parameters of a eutectic solidification PF model is more difficult than estimating the parameters of a solidification PF model with a simple geometry using DA. Therefore, we compared the DA conditions with those in previous studies [34,37], in which DA for the solidification PFM of isomorphous alloys was conducted.

We applied the EnKF to unidirectional solidification PF simulations of eutectic alloys and demonstrated its effectiveness in the twin experiments. The simultaneous estimation of four PF simulation parameters (i.e., PF interface mobility, solute mobility, anisotropy strength, and gradient energy coefficient) was possible using appropriate DA conditions ($N_{\text{ens}} = 100$; filtering interval $\Delta t_{\text{filt}} = 50$, 30 steps). Recalculation using the PF simulation parameters estimated by EnKF reproduced the results of the PF calculations using the true values. The results of the twin experiments suggested that the observation frequency of the observation data is necessary for the DA. The eutectic system had almost no effect on the estimation conditions of the DA. Further, parameter
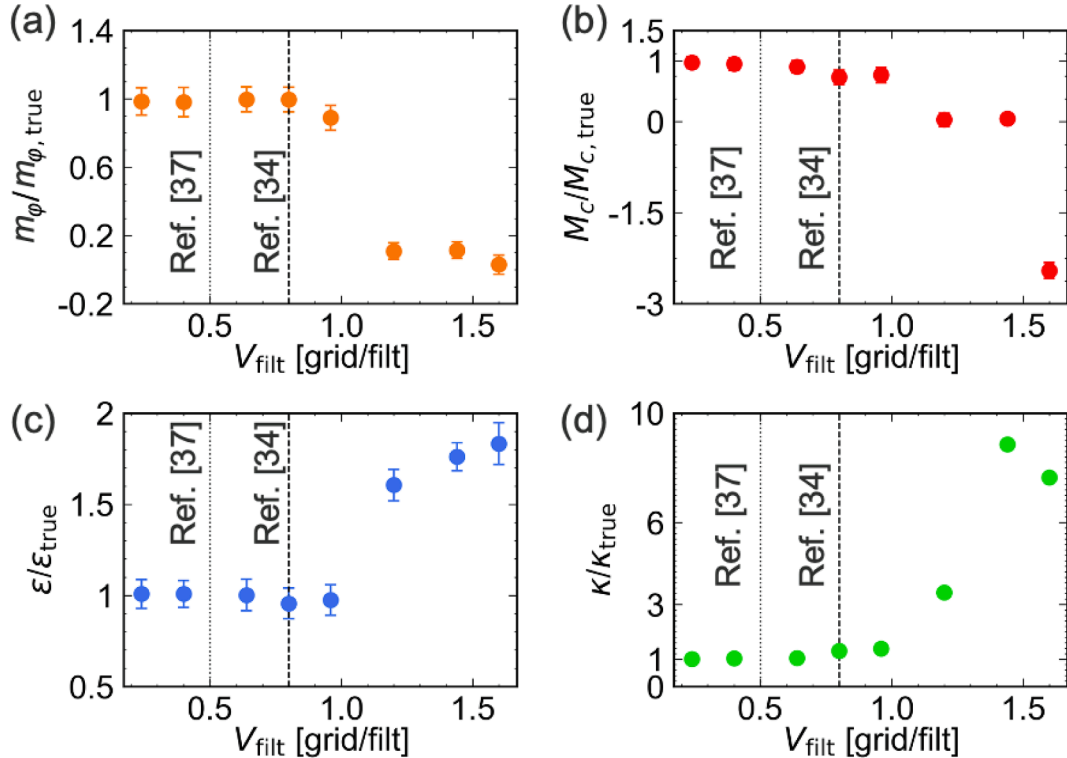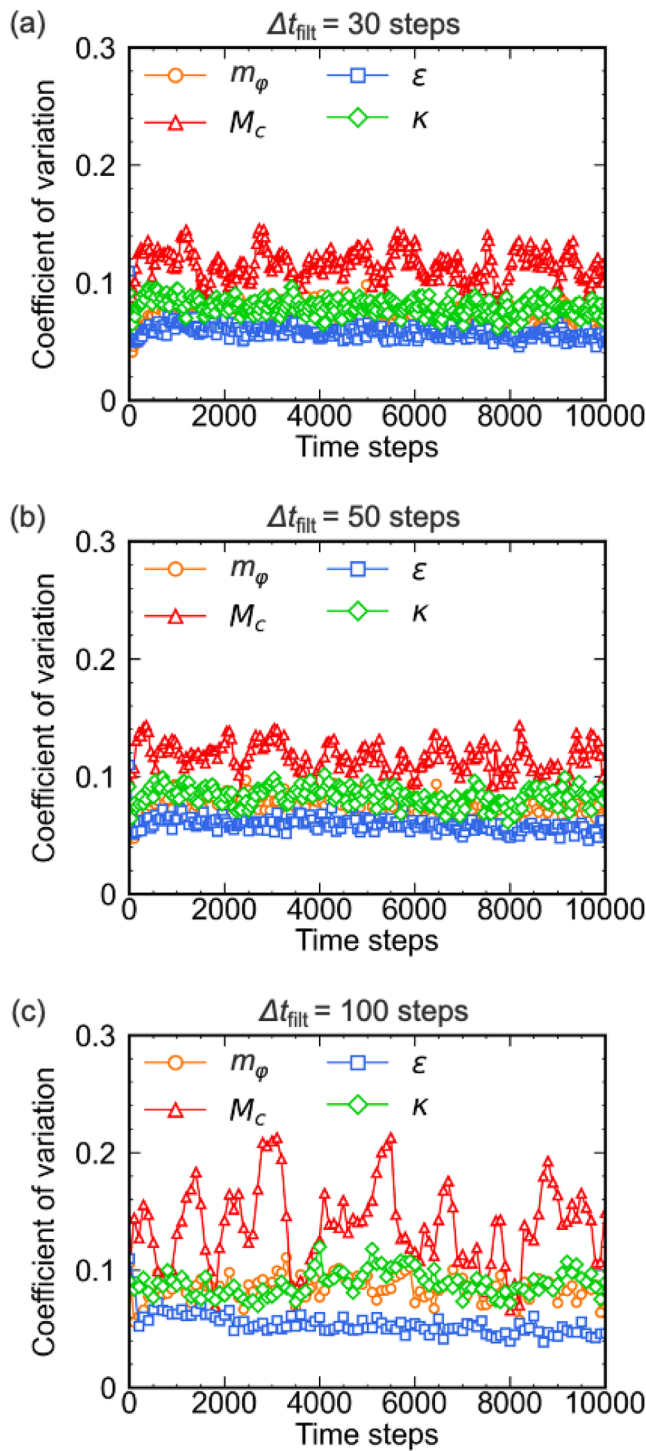

Fig. 7. Estimation accuracy of (a) phase-field mobility, (b) solute mobility, (c) anisotropy strength, and (d) gradient energy coefficient as a function of V_{filt}. The dashed and dotted lines represent V_{filt} in Refs. [34,37], respectively.

Fig. 8. Comparison of the time variation of CVs of the estimated parameters in each twin experiment with different Δt_{filt} of (a) 30, (b) 50, and (c) 100 steps.

estimation by the DA could be performed under the same conditions as those for other systems reported in previous studies. We found that the optimum Δt_{filt} can be understood in terms of solid–liquid interfacial velocity. In the future, PF simulation parameters will be estimated through DA using in-situ observation images as observation data.

Author contributions

M.O. and Y.K. conceptualized the study. Y.S. performed the data assimilation combined phase-field simulations. C.Z. and A.Y. helped with the analyses of the results of the phase-field simulations. Y.S., M.O., C.Z., A.Y., and Y.K. interpreted the results. All authors reviewed and commented on the paper.

CRediT authorship contribution statement

Yusuke Seguchi: Writing – original draft, Visualization, Validation, Software, Methodology, Investigation, Formal analysis, Data curation. **Masayuki Okugawa:** Writing – original draft, Visualization, Validation, Supervision, Software, Project administration, Methodology, Funding acquisition, Conceptualization. **Chuanqi Zhu:** Writing – review & editing, Validation, Software, Formal analysis, Data curation. **Akinori Yamanaka:** Writing – review & editing, Validation, Software, Methodology. **Yuichiro Koziumi:** Writing – review & editing, Validation, Supervision, Project administration, Methodology, Funding acquisition, Conceptualization.

Declaration of competing interest

The authors declare that they have no known competing financial interests or personal relationships that could have appeared to influence the work reported in this paper.

Data availability

Data will be made available on request.

Appendix A. Supplementary material

Supplementary data to this article can be found online at https://doi.org/10.1016/j.commatsci.2024.112910.

References

[1] L. Luo, C. Wei, X.M. Li, X. Wang, Research on microstructure evolution of Al-Al$_2$Cu eutectic by regional melting under directional solidification, Cryst. Res. Technol. 54 (2019) 1900108, https://doi.org/10.1002/crat.201900108.

[2] S.A. Souza, C.T. Rios, A.A. Coelho, P.L. Ferrandini, S. Gama, R. Caram, Growth and morphological characterization of Al-Cr-Nb eutectic alloys, J. Alloys Compd. 402 (2005) 156–161, https://doi.org/10.1016/j.jallcom.2005.04.137.

[3] D.A. Pawlak, K. Kolodziejak, S. Turczynski, J. Kisielewski, K. Rożniatowski, R. Diduszko, M. Kaczkan, M. Malinowski, Self-organized, rodlike, micrometer-scale microstructure of Tb3Sc2Al3O12-TbScO3: Pr eutectic, Chem. Mater. 18 (2006) 2450–2457, https://doi.org/10.1021/cm060136h.

[4] D.A. Pawlak, K. Kolodziejak, K. Rozniatowski, R. Diduszko, M. Kaczkan, M. Malinowski, M. Piersa, J. Kisielewski, T. Lukasiewicz, PrAlO$_3$-PrAl$_{11}$O$_{18}$ eutectic: its microstructure and spectroscopic properties, Cryst. Growth. Des. 8 (2008) 1243–1249, https://doi.org/10.1021/cg0609522.

[5] S. Moniri, H. Bale, T. Volkenandt, Y. Wang, J. Gao, T. Lu, K. Sun, R.O. Ritchie, A. J. Shahani, Multi-step crystallization of self-organized spiral eutectics, Small 16 (2020) 1906146, https://doi.org/10.1002/smll.201906146.

[6] S. Akamatsu, M. Perrut, S. Bottin-Rousseau, G. Faivre, Spiral two-phase dendrites, Phys. Rev. Lett. 104 (2010) 056101. 0.1103/PhysRevLett.104.056101.

[7] S. Lee, J. Kim, S. Hong, H. Park, J. Park, N. Lee, Y. Seo, J. Suh, J. Eckert, D. Kim, J. Park, K. Kim, Micro-to-nano-scale deformation mechanisms of a bimodal ultrafine eutectic composite, Sci. Rep. 4 (2014) 6500, https://doi.org/10.1038/srep06500.

[8] X. Jin, J. Bi, L. Zhang, Y. Zhou, X. Du, Y. Liang, B. Li, A new CrFeNi$_2$Al eutectic high entropy alloy system with excellent mechanical properties, J. Alloys Compd. 770 (2019) 655–661, https://doi.org/10.1016/j.jallcom.2018.08.176.

[9] K. Kamada, Y. Takizawa, M. Yoshino, N. Kutsuzawa, K.J. Kim, R. Murakami, V. V. Kochurikhin, A. Yoshikawa, Growth and scintillation properties of Eu doped

Li$_2$SrCl$_4$/LiSr$_2$Cl$_5$ eutectic, J. Cryst. Growth 581 (2022) 126500, https://doi.org/10.1016/j.jcrysgro.2021.126500.

[10] Y. Ohashi, N. Yasui, Y. Yokota, A. Yoshikawa, T. Den, Submicron-diameter phase-separated scintillator fibers for high-resolution X-ray imaging, Appl. Phys. Lett. 102 (2013) 051907, https://doi.org/10.1063/1.4790295.

[11] D.A. Pawlak, S. Turczynski, M. Gajc, K. Kolodziejak, R. Diduszko, K. Rozniatowski, J. Smalc, I. Vendik, How far are we from making metamaterials by self-organization? the microstructure of highly anisotropic particles with an SRR-like geometry, Adv. Funct. Mater. 20 (2010) 1116–1124, https://doi.org/10.1002/adfm.200901875.

[12] M. Ginibre, S. Akamatsu, G. Faivre, Experimental determination of the stability diagram of a lamellar eutectic growth front, Phys. Rev. E 56 (1997) 780–796, https://doi.org/10.1103/physreve.56.780.

[13] C.D. Rosa, C. Park, E.L. Thomas, B. Lotz, Microdomain patterns from directional eutectic solidification and epitaxy, Nature 405 (2000) 433–437, https://doi.org/10.1038/35013018.

[14] A.A. Kulkarni, E. Hanson, R. Zhang, K. Thornton, P.V. Braun, Archimedean lattices emerge in template-directed eutectic solidification, Nature 577 (2020) 355–358, https://doi.org/10.1038/s41586-019-1893-9.

[15] A.J. Shahani, X. Xiao, P.W. Voorhees, The mechanism of eutectic growth in highly anisotropic materials, Nat. Commun. 7 (2016) 12953, https://doi.org/10.1038/ncomms12953.

[16] R. Goetzinger, M. Barth, D.M. Herlach, Mechanism of formation of the anomalous eutectic structure in rapidly solidified Ni–Si, Co–Sb and Ni–Al–Ti alloys, Acta Mater. 46 (1998) 1647–1655, https://doi.org/10.1016/S1359-6454(97)00339-X.

[17] Y. Watanabe, S. Oike, Formation mechanism of graded composition in Al–Al$_2$Cu functionally graded materials fabricated by a centrifugal in situ method, Acta Mater. 53 (2005) 1631–1641, https://doi.org/10.1016/j.actamat.2004.12.013.

[18] C. Gu, M.P. Moodispaw, A.A. Luo, Cellular automaton simulation and experimental validation of eutectic transformation during solidification of Al-Si alloys, npj Comput. Mater. 8 (2022) 134, https://doi.org/10.1038/s41524-022-00824-5.

[19] L. Rátkai, G.I. Tóth, L. Környei, T. Pusztai, L. Gránásy, Phase-field modeling of eutectic structures on the nanoscale: the effect of anisotropy, J. Mater. Sci. 52 (2017) 5544–5558, https://doi.org/10.1007/s10853-017-0853-8.

[20] M. Kellner, S.N. Enugala, B. Nestler, Modeling of stoichiometric phases in off-eutectic compositions of directional solidifying NbSi-10Ti for phase-field simulations, Comput. Mater. Sci. 203 (2022) 111046, https://doi.org/10.1016/j.commatsci.2021.111046.

[21] M. Seiz, M. Kellner, B. Nestler, Simulation of dendritic–eutectic growth with the phase-field method, Acta Mater. 254 (118965) (2023) 118965, https://doi.org/10.1016/j.actamat.2023.118965.

[22] R. Kobayashi, Modeling and numerical simulations of dendritic crystal growth, Physica D 63 (1993) 410–423, https://doi.org/10.1016/0167-2789(93)90120-P.

[23] C. Zhu, Y. Seguchi, M. Okugawa, C. Guo, Y. Koizumi, Influences of growth front surfaces on the grain boundary development of multi-crystalline silicon during directional solidification: 2D/3D multi-phase-field study, Mater. 27 (2023) 101702, https://doi.org/10.1016/j.mtla.2023.101702.

[24] M. Okugawa, Y. Ohigashi, Y. Furishiro, Y. Koizumi, T. Nakano, Equiaxed grain formation by intrinsic heterogeneous nucleation via rapid heating and cooling in additive manufacturing of aluminum-silicon hypoeutectic alloy, J. Alloys Compd. 919 (2022) 165812, https://doi.org/10.1016/j.jallcom.2022.165812.

[25] M. Okugawa, Y. Furushiro, Y. Koizumi, Effect of rapid heating and cooling conditions on microstructure formation in powder bed fusion of Al-Si hypoeutectic alloy: A phase-field study, Materials (basel) 15 (2022) 6092, https://doi.org/10.3390/ma15176092.

[26] M. Okugawa, D. Izumikawa, Y. Koizumi, Simulations of non-equilibrium and equilibrium segregation in nickel-based superalloy using modified Scheil-Gulliver and phase-field methods, Mater. Trans. 61 (2020) 2072–2078, https://doi.org/10.2320/matertrans.MT-MA2020005.

[27] H. Iwaizako, M. Okugawa, K. Saito, Y. Koizumi, A. Chiba, Y. Tachiya, M. Ohnuma, K. Kuritani, Spinodal decomposition in plastically deformed Fe–Cr–Co magnet alloy, ISIJ Int. 62 (2022) 1268–1274, https://doi.org/10.2355/isijinternational.ISIJINT-2021-441.

[28] G. Boussinot, M. Döring, M. Schmidt, M. Apel, Strongly out-of-equilibrium growth morphologies in fast solidifying eutectics, Phys. Rev. Materials 6 (2022) 043405, https://doi.org/10.1103/PhysRevMaterials.6.043405.

[29] E. Miyoshi, T. Takaki, M. Ohno, Y. Shibuta, S. Sakane, T. Shimokawabe, T. Aoki, Ultra-large-scale phase-field simulation study of ideal grain growth, npj Comput. Mater. 3 (2017) 25, https://doi.org/10.1038/s41524-017-0029-8.

[30] K. Wang, G. Boussinot, C. Hüter, E.A. Brener, R. Spatschek, Modeling of dendritic growth using a quantitative nondiagonal phase field model, Phys. Rev. Materials 4 (2020) 033802, https://doi.org/10.1103/PhysRevMaterials.4.033802.

[31] G. Evensen, The Ensemble Kalman Filter: theoretical formulation and practical implementation, Ocean Dyn. 53 (2003) 343–367, https://doi.org/10.1007/s10236-003-0036-9.

[32] F. Rabier, H. Järvinen, E. Klinker, J.-F. Mahfouf, A. Simmons, A., The ECMWF operational implementation of four-dimensional variational assimilation. I: Experimental results with simplified physics, Q. J. r. Meteorol. Soc. 126 (2000) 1143–1170, https://doi.org/10.1002/qj.49712656415.

[33] A. Yamanaka, K. Takahashi, Data assimilation for three-dimensional phase-field simulation of dendritic solidification using the local ensemble transform Kalman filter, Mater. Today Commun. 25 (2020) 101331, https://doi.org/10.1016/j.mtcomm.2020.101331.

[34] M. Ohno, Y. Oka, S. Sakane, Y. Shibuta, T. Takaki, Bayesian inference of solid-liquid interfacial properties out of equilibrium, Phys. Rev. E 101 (2020) 052121, https://doi.org/10.1103/PhysRevE.101.052121.

[35] E. Miyoshi, M. Ohno, Y. Shibuta, A. Yamanaka, T. Takaki, Novel estimation method for anisotropic grain boundary properties based on Bayesian data assimilation and phase-field simulation, Mater. Des. 210 (2021) 110089, https://doi.org/10.1016/j.matdes.2021.110089.

[36] A. Yamanaka, Y. Maeda, K. Sasaki, Ensemble Kalman filter-based data assimilation for three-dimensional multi-phase-field model: Estimation of anisotropic grain boundary properties, Mater. Des. 165 (2019) 107577, https://doi.org/10.1016/j.matdes.2018.107577.

[37] Y. Nagatsuma, M. Ohno, T. Takaki, Y. Shibuta, Bayesian data assimilation of temperature dependence of solid–liquid interfacial properties of nickel, Nanomaterials 11 (2021) 2308, https://doi.org/10.3390/nano11092308.

[38] K. Sasaki, A. Yamanaka, S. Ito, H. Nagao, Data assimilation for phase-field models based on the ensemble Kalman filter, Comput. Mater. Sci. 141 (2018) 141–152, https://doi.org/10.1016/j.commatsci.2017.09.025.

[39] C. Zhu, J. Yamamoto, Y. Koizumi, K. Yuge, K. Kishida, H. Inui, Comprehensive phase-field study on directionally solidified MoSi$_2$/Mo$_5$Si$_3$ eutectic alloy, Mater. Sci. Forum. 1016 (2021) 749–754, https://doi.org/10.4028/www.scientific.net/MSF.1016.749.

[40] C. Zhu, Y. Koizumi, A. Chiba, K. Yuge, K. Kishida, H. Inui, Pattern formation mechanism of directionally solidified MoSi$_2$/Mo$_5$Si$_3$ eutectic by phase-field simulation, Intermetallics 116 (2020) 106590, https://doi.org/10.1016/j.intermet.2019.106590.

[41] A. Artemev, Y. Jin, A.G. Khachaturyan, Three-dimensional phase field model of proper martensitic transformation, Acta Mater. 49 (2001) 1165–1177, https://doi.org/10.1016/S1359-6454(01)00021-0.

[42] Y.H. Wen, L.Q. Chen, P.M. Hazzledine, Y. Wang, A three-dimensional phase-field model for computer simulation of lamellar structure formation in γ TiAl intermetallic alloys, Acta Mater. 49 (2001) 2341–2353, https://doi.org/10.1016/S1359-6454(01)00014-3.

[43] J. A. Dantzig, M. Rappaz, Solidification second ed., (École Polytechnique Fédérale de Lausanne Press, (2009).

[44] S.M. Allen, J.W. Cahn, A microscopic theory for antiphase boundary motion and its application to antiphase domain coarsening, Acta Metall. 27 (1979) 1085–1095, https://doi.org/10.1016/0001-6160(79)90196-2.

[45] J.W. Cahn, J.E. Hilliard, Free energy of a nonuniform system. I. Interfacial free energy, J. Chem. Phys. 28 (1958) 258–267, https://doi.org/10.1063/1.1744102.

[46] J. Crank, P. Nicolson, A practical method for numerical evaluation of solutions of partial differential equations of heat conduction type, Proc. Camb. Phil. Soc. 43 (1947) 50–67, https://doi.org/10.1007/BF02127704.

[47] J.G. Charney, R. Fjørtoft, J. von Neumann, Numerical integration of the barotropic vorticity equation, Tellus 2 (1950) 237–254, https://doi.org/10.1111/j.2153-3490.1950.tb00336.x.

[48] M. Şerefoğlu, S. Bottin-Rousseau, S. Akamatsu, Lamella-rod pattern transition and confinement effects during eutectic growth, Acta Mater. 242 (2023) 118425, https://doi.org/10.1016/j.actamat.2022.118425.

[49] S. Akamatsu, T. Ihle, Similarity law for the tilt angle of dendrites in directional solidification of non-axially-oriented crystals, Phys. Rev. E 56 (1997) 4479–4485, https://doi.org/10.1103/PhysRevE.56.4479.

[50] V.T. Witusiewicz, L. Sturz, U. Hecht, S. Rex, Lamellar coupled growth in the neopentylglycol-(D)camphor eutectic, J. Cryst. Growth 386 (2014) 69–75, https://doi.org/10.1016/j.jcrysgro.2013.09.035.

[51] V.T. Witusiewicz, U. Hecht, S. Rex, In-situ observation of eutectic growth in Al-based alloys by light microscopy, J. Cryst. Growth 372 (2013) 57–64, https://doi.org/10.1016/j.jcrysgro.2013.02.033.

[52] L.C. Chuang, K. Maeda, K. Morito, K. Fujiwara, In situ observation of solidification and subsequent evolution of Ni-Si eutectics, Scr. Mater. 211 (2022) 114513, https://doi.org/10.1016/j.scriptamat.2022.114513.

[53] G. Reinhart, D.J. Browne, F. Kargl, F. García-Moreno, M. Becker, E. Sondermann, K. Binder, J.S. Mullen, G. Zimmermann, R.H. Mathiesen, W.H. Sillekens, H. Nguyen-Thi, In-situ X-ray monitoring of solidification and related processes of metal alloys, NPJ Microgravity 9 70 (2023), https://doi.org/10.1038/s41526-023-00321-z.

[54] Z. Song, O.V. Magdysyuk, T. Sparks, Y.L. Chiu, B. Cai, Revealing growth mechanisms of faceted Al$_2$Cu intermetallic compounds via high-speed Synchrotron X-ray tomography, Acta Mater. 231 (2022) 117903, https://doi.org/10.1016/j.actamat.2022.117903.

[55] Y. Kobayashi, K. Dobara, H. Todoroki, C. Nam, K. Morishita, H. Yasuda, *In-situ* measurements of solute partition coefficients between solid and liquid phases in Fe–Cr–Ni–Mo–Cu alloys during solidification, ISIJ Int. 60 (2020) 276–285, https://doi.org/10.2355/isijinternational.ISIJINT-2019-444.

[56] S. Feng, E. Liotti, M.D. Wilson, L. Jowitt, P.S. Grant, In situ mapping of chemical segregation using synchrotron x-ray imaging, MRS Bulletin. 45 (2020) 934–942, https://doi.org/10.1557/mrs.2020.270.

[57] H. Yasuda, K. Morishita, N. Nakatsuka, T. Nishimura, M. Yoshiya, A. Sugiyama, K. Uesugi, A. Takeuchi, Dendrite fragmentation induced by massive-like δ–γ transformation in Fe–C alloys, Nat. Commun. 10 (2019) 3183, https://doi.org/10.1038/s41467-019-11079-y.

[58] A. Kulovits, J.M.K. Wiezorek, T. Lagrange, B.W. Reed, G.H. Campbell, Revealing the transient states of rapid solidification in aluminum thin films using ultrafast in situ transmission electron microscopy, Philos. Mag. Lett. 91 (2011) 287–296, https://doi.org/10.1080/09500839.2011.558030.

[59] J.T. McKeown, A.K. Kulovits, C. Liu, K. Zweiacker, B.W. Reed, T. Lagrange, J.M. K. Wiezorek, G.H. Campbell, In situ transmission electron microscopy of crystal growth-mode transitions during rapid solidification of a hypoeutectic Al-Cu alloy, Acta Mater. 65 (2014) 56–68, https://doi.org/10.1016/j.actamat.2013.11.046.

[60] V. Bathula, C. Liu, K. Zweiacker, J.T. McKeown, J.M.K. Wiezorek, Interface velocity dependent solute trapping and phase selection during rapid solidification of laser melted hypo-eutectic Al-11at.%Cu alloy, Acta Mater. 195 (2020) 341–357, https://doi.org/10.1016/j.actamat.2020.04.006.

[61] J.T. McKeown, K. Zweiacker, C. Liu, D.R. Coughlin, A.J. Clarke, J.K. Baldwin, J. W. Gibbs, J.D. Roehling, S.D. Imhoff, P.J. Gibbs, D. Tourret, J.M.K. Wiezorek, G. H. Campbell, Time-resolved in situ measurements during rapid alloy solidification: experimental insight for additive manufacturing, JOM 68 (2016) 985–999, https://doi.org/10.1007/s11837-015-1793-x.